Generalizing the effects of chirality on block copolymer assembly

Hsiao-Fang Wang[a], Kai-Chieh Yang[a], Wen-Chun Hsu[a], Jing-Yu Lee[b], Jung-Tzu Hsu[b], Gregory M. Grason[c], Edwin L. Thomas[d], Jing-Cherng Tsai[b,1], and Rong-Ming Ho[a,1]

[a]Department of Chemical Engineering, National Tsing Hua University, Hsinchu 30013, Taiwan; [b]Department of Chemical Engineering, National Chung Cheng University, Chia-Yi 62142, Taiwan; [c]Department of Polymer Science and Engineering, University of Massachusetts, Amherst, MA 01003; and [d]Department of Materials Science and NanoEngineering, Rice University, Houston, TX 77005

Edited by Tim Lodge, University of Minnesota, Minneapolis, MN, and accepted by Editorial Board Member Thomas E. Mallouk January 8, 2019 (received for review July 18, 2018)

We explore the generality of the influence of segment chirality on the self-assembled structure of achiral–chiral diblock copolymers. Poly(cyclohexylglycolide) (PCG)-based chiral block copolymers (BCPs*), poly(benzyl methacrylate)-*b*-poly(D-cyclohexylglycolide) (PBnMA-PDCG) and PBnMA-*b*-poly(L-cyclohexyl glycolide) (PBnMA-PLCG), were synthesized for purposes of systematic comparison with polylactide (PLA)-based BCPs*, previously shown to exhibit chirality transfer from monomeric unit to the multichain domain morphology. Opposite-handed PCG helical chains in the enantiomeric BCPs* were identified by the vibrational circular dichroism (VCD) studies revealing transfer from chiral monomers to chiral intrachain conformation. We report further VCD evidence of chiral interchain interactions, consistent with some amounts of handed skew configurations of PCG segments in a melt state packing. Finally, we show by electron tomography [3D transmission electron microscope tomography (3D TEM)] that chirality at the monomeric and intrachain level ultimately manifests in the symmetry of microphase-separated, multichain morphologies: a helical phase (H*) of hexagonally, ordered, helically shaped tubular domains whose handedness agrees with the respective monomeric chirality. Critically, unlike previous PLA-based BCP*s, the lack of a competing crystalline state of the chiral PCGs allowed determination that H* is an equilibrium phase of chiral PBnMA-PCG. We compared different measures of chirality at the monomer scale for PLA and PCG, and argued, on the basis of comparison with mean-field theory results for chiral diblock copolymer melts, that the enhanced thermodynamic stability of the mesochiral H* morphology may be attributed to the relatively stronger chiral intersegment forces, ultimately tracing from the effects of a bulkier chiral side group on its main chain.

chirality effects | homochiral evolution | self-assembly | chiral block copolymers | helical phase

Self-assembly is a process by which molecular or particulate subunits spontaneously organize into well-defined multiunit structures (1, 2). Nature uses self-assembly to build a diverse range of functional intracellular and extracellular architectures in living organisms. One common theme of biological assembly is the templating of hierarchical structure through the molecular-scale symmetry and interactions of chiral constituents (3). For example, chirality transfer from protein building blocks to twisted intermolecular arrangements—characterized by chirality at length scales much larger than those blocks—underlies functional optical and mechanical structures found in organisms from insects to mollusks (4, 5). The remarkable and adaptable properties of these mesochiral architectures have inspired numerous attempts to recapitulate them, and their functional properties, in synthetic materials (6, 7).

Critical to the "bottom-up" process of mesochiral assembly in biological systems is the transfer and manifestation of chirality at multiple scales: from the symmetry of amino acid residues, to chiral (e.g., alpha helical) secondary and tertiary structure, and ultimately the chiral patterns of multiprotein packing extending to cellular and intercellular length scales. In this paper, we describe the manifestation of hierarchical chirality in the self-assembly of block copolymers (BCPs), a synthetic class of materials whose combination of chemical versatility and morphological complexity have facilitated extensive studies of the relationship between their molecular properties and self-assembly behavior. In the canonical self-consistent field model (8), the equilibrium structures of BCPs are well understood to be controlled by a relatively small number of parameters describing the number of flexible segments in the chain, the segment sizes and volume fractions of chemically unlike blocks, and their relative immiscibilities, characterized by the Flory-Huggins chi(χ)-parameters. Extensive experimental study of BCP assembly generally confirms the relationship between molecular structure and the complex array of periodically ordered phases predicted from canonical BCP assemblies: in the simplest case of linear diblocks, lamellae (L), double gyroid (DG), hexagonally packed cylinder (HC), and BCC spheres (S).

Recent studies of diblocks that incorporate blocks with stereopure polymeric backbones have shown that chirality has an impact on the self-assembly that falls outside of the traditional BCP paradigm. Notably, solution-cast assembly of polystyrene-*b*-poly(D or L-lactide) (PS-PDLA or PS-PLLA) diblocks gave rise

Significance

Chirality is a measure of asymmetry that is important in many branches of science. Homochiral evolution at different length scales is critical for molecular processes in nature (such as communication, replication, and enzyme catalysis) that rely on a delicate balance between molecular and conformational chirality and, most importantly, control the nature of the self-assembly of superstructures of constituent molecules. Here, we compare the homochiral evolution from molecular, to intrachain, to interchain, and, ultimately, to mesodomain chirality from the self-assembly of a pair of block copolymers possessing a chiral block that exhibits one of the two different stereochemistries. The comparison sheds light on the physical mechanisms that link chiral structure across these length scales in this prototypical class of self-assembling materials.

Author contributions: H.-F.W., W.-C.H., J.-Y.L., J.-C.T., and R.-M.H. designed research; H.-F.W., K.-C.Y., W.-C.H., J.-T.H., J.-C.T., and R.-M.H. performed research; H.-F.W. and R.-M.H. contributed new reagents/analytic tools; H.-F.W., K.-C.Y., W.-C.H., J.-T.H., G.M.G., E.L.T., J.-C.T., and R.-M.H. analyzed data; and H.-F.W., G.M.G., E.L.T., J.-C.T., and R.-M.H. wrote the paper.

Conflict of interest statement: The authors are the inventors of a provisional patent application filed by the National Tsing Hua University related to the results reported here.

This article is a PNAS Direct Submission. T.L. is a guest editor invited by the Editorial Board.

Published under the PNAS license.

[1]To whom correspondence may be addressed. Email: rmho@mx.nthu.edu.tw or chmjct@ccu.edu.tw.

This article contains supporting information online at www.pnas.org/lookup/suppl/doi:10.1073/pnas.1812356116/-/DCSupplemental.

Published online February 14, 2019.

Downloaded by guest on January 10, 2020

to form the so-called helical phase (H*), hexagonally packed arrays of helical cylinders whose homochiral helical sense is dictated by monomer stereochemistry (9, 10). Subsequent spectroscopic studies of these chiral diblocks and their assembly demonstrated the transfer of chirality from monomer stereochemistry to the intrachain helicity of PDLA or PLLA blocks (11, 12), and suggested further chirality in the interchain pattern of organization in H* assemblies. Motivated by these observations, Grason and coworkers developed a generalization of the standard self-consistent field model of BCPs, named orientational self-consistent field (oSCF) theory, which models chirality as a thermodynamic preference for cholesteric twist of the flexible chain segments. The oSCF introduced two new parameters to the equilibrium model of chiral block copolymer (BCP*), the Frank elastic constants for gradients in the orientational texture of chiral block segments, and inverse pitch, $q_0 = 2\pi/p$, where p is the preferred intersegment pitch of the cholesteric helix (13); it is a measure of the chirality biased intersegment skew angle preferred by interchain forces between (helical) chain segments. This theory predicts that, for large enough q_0, H* is an equilibrium phase of BCP*s, stabilized by cholesteric packing threaded through the helical domain core. Notwithstanding this apparent agreement between oSCF theory and experimental observations of H* in chiral polylactide (PLA)-based diblocks (i.e., the observed chiral mesodomain shapes are predicted to be equilibrium phases in some parameter regime), a systematic understanding of the chirality transfer mechanism in these systems has remained elusive. Foremost, the equilibrium formation of the H* in the PLA-based BCPs* is significantly limited by the highly crystallizable nature of the chiral PLA blocks, typically requiring a nonequilibrium processing pathway to quench the chiral diblock in a noncrystalline state of PLA (14–16). Indeed, long-time, thermal annealing of PS-PLLA above the solidification temperatures of both blocks causes a phase transformation from H* to DG (an apparently achiral form), indicating that H* may be only a metastable phase of PS-P(D or L)LA (9, 17). A transient H* phase could be also formed by self-assembling poly(4-vinylpyridine)-*b*-poly(L-lactide) (P4VP-PLLA), suggesting that the mechanism of chirality transfer to the domain shape is not specific to the achiral block. However, a phase transformation of H* into HC was achieved by slow solvent evaporation, indicating that the mesochiral H* may be kinetically trapped in the P4VP-PLLA system as well.

In this paper, we demonstrate the chirality transfer from an enantiomeric polymer backbone to the mesochiral domain shape beyond the PLA-specific chemistries studied to date, and thus suggest that such effects may be generic. We first describe the synthesis and characterization of a BCP* system, poly(cyclohexylglycolide) (PCG)-based BCP*. As shown in Fig. 1, the structure of the chiral PCG block is similar to chiral PLA, but with the methyl side groups of the lactide replaced with bulkier aromatic rings. We show that this change in monomeric structure preserves and possibly enhances the effects of chirality transfer, and moreover, wholly suppresses crystallization of the chiral PCG, allowing the influence of crystallization of the chiral block on the mesodomain formation to be strictly ruled out, allowing long-time, high-temperature annealing without intervening crystallization to test the thermodynamic stability of the H* phase. Circular dichroism measurements verify the transfer of monomeric chirality (i.e., chiral hexahydromandelic acids) to intrachain conformations of chiral PCG homopolymers. We argue that a relatively higher rotational strength of chiral PCG relative to chiral PLA may be indicative to stronger tendencies to transfer monomeric chirality to higher length scales, specifically to more persistent helical intrachain conformations, and, ultimately, to more prominent chiral intersegment interactions, of the type hypothesized to drive H* formation (18). To test the assembly behavior, a chiral diblock was prepared by combining chiral PCG with an achrial poly(benzyl methacrylate) (PBnMA) block. Comparative estimates of the solubilities of these blocks suggest that the χ parameter of a poly(benzyl methacrylate)-*b*-poly(D-cyclohexylglycolide) (PBnMA-PDCG) diblocks (Fig. 1*A*) is comparable to the better studied polystyrene-*b*-poly(D-lactide) (PS-PDLA) systems (Fig. 1*B*), allowing us to focus on the primary impacts of a noncrystalline and bulkier chiral side group chemistry on the resulting self-assembly behavior. The PBnMA-PDCG H* phase is stable upon long-time, high-temperature thermal annealing, demonstrating that (*i*) multiple chiral chain chemistries can drive the H* mesochiral domain pattern and (*ii*) that H* is an equilibrium phase of chiral diblocks, consistent with theoretical predictions. Finally, we describe vibrational circular dichroism (VCD) measurements of PCG homopolymers that give evidence of chiral interchain backbone packing in the self-assembled H*, consistent with the hypothesis that chiral mesodomain textures of twisted (i.e., cholesteric) segment packing play a key role in the chirality transfer mechanism from chiral monomer to mesodomain shape in BCP* assembly.

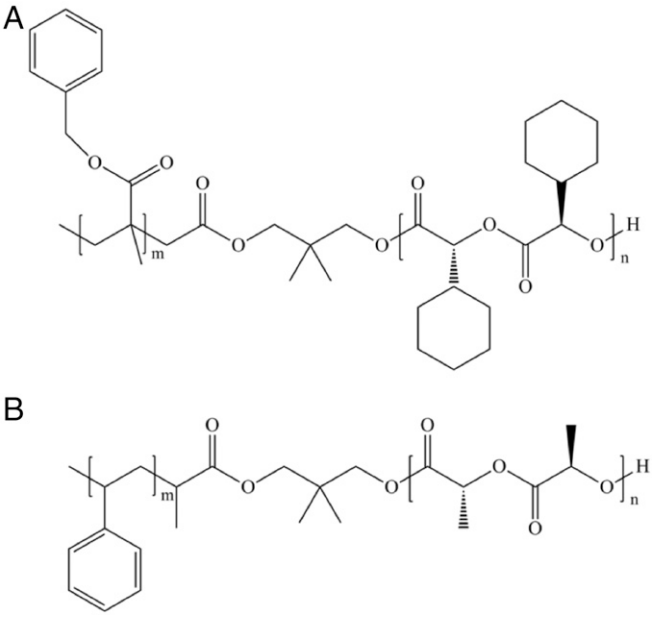

Fig. 1. Chemical structures of BCPs*: (*A*) PBnMA-PDCG; (*B*) PS-PDLA BCPs*.

Results and Discussion

Synthesis of Enantiomeric PBnMA-PCG BCPs*. To examine the generality of the impact of chirality on the self-assembly of BCPs*, we designed and synthesized a type of BCP*. On the basis of molecular structure, mandelic acid is an ideal candidate because the stereostructure is similar to lactic acid, but the methyl group of the latter chain is replaced by the bulkier group ring carbon in the former. Intuitively, this bulkier side group increases the asymmetry of the chiral carbon, enhancing structural chirality of the monomer as we show below. However, we find that it is not possible to prepare stereopure poly(mandelic acid) from a direct ring-opening polymerization of chiral mandelide (dimeric mandelic acid). As described in *SI Appendix* (*SI Appendix*, Scheme S1), ring-opening polymerization leads to racemization of phenyl groups on mandelic acid monomers, resulting in an achiral polymer, or otherwise, a poor control over enantiomer purity. To solve the problem of racemization, we first performed hydrogenation of chiral mandelic acid, converting the phenyl group into a cyclohexyl group, yielding chiral hexahydromandelic acid (HHMA). Chiral dicyclohexylglycolide (dimer of HHMA) was then polymerized through a ring-opening reaction to achieve stereopure chiral PCG (19). We synthesized enantiomeric PBnMA-PCG BCPs*

Downloaded by guest on January 10, 2020

by atom transfer radical polymerization and living ring-opening polymerization in sequence, starting from the bifunctional initiator as illustrated in Fig. 2 (see *SI Appendix* for details). Table 1 summarizes the characterization of the samples examined in this study. Notably, the choice of the achiral PBnMA with the chiral PCG is to create a diblock system having interaction parameter equivalent to the one from the achiral PS and the chiral PLA, giving systematic comparison of twisting power effects on thermodynamic stability of forming H* phase.

Conformational Chirality of Chiral PCGs and PBnMA-PCG BCPs*. Fig. 3*A* shows the electronic circular dichroism (ECD) and corresponding absorption spectra of the chiral HHMAs in dilute solutions, indicating molecular chirality of the monomeric building blocks. For L-hexahydromandelic acid (L-HHMA), a positive ECD signal appears at 224 nm, which is the characteristic absorption band for the n → π* transition of carboxylic group (O=C–OH), with the ECD spectra of D-hexahydromandelic acid (D-HHMA) appearing as mirror image of the L-HHMA results. ECD measurements of the chiral PCG homopolymer in dichloromethane and PCG-based BCPs* in dilute *p*-dioxane are shown in Fig. 3 *B* and *C* (note that *p*-dioxane is used for solubility of the PCG-based BCPs). Appearance of ECD signals at the same wavelengths indicates that the chirality of the monomer is preserved in the polymeric forms of PCG.

Having confirmed the monomeric chirality in the chain backbone, we use VCD to test whether this chirality transfers to intermonomer arrangements along chains, specifically intrachain rotation of side group along the backbone. Fig. 4*A* shows the VCD and corresponding absorption spectra of PDCG homopolymers in dilute dichloromethane solution. VCD probes the vibrational coupling between two chromophores, say *i* and *j*, with transition electron dipoles $\boldsymbol{\mu}_i$ and $\boldsymbol{\mu}_j$, respectively, and spatial separation $\mathbf{R}_{ij}$. According to the interchromophore coupling model, a VCD contribution from a particular chromophore pair is proportional to the pseudoscalar quantity $\Delta_{ij} = (\boldsymbol{\mu}_i \times \boldsymbol{\mu}_j) \cdot \mathbf{R}_{ij}$ (20). Hence, if the signal is nonzero, then the average of Δ_{ij} (i.e., the conformational distribution weighted by interchromophore coupling strength) is nonzero, indicating a chiral bias in the interchromophore skew (i.e., the rotation angle between $\boldsymbol{\mu}_i$ and $\boldsymbol{\mu}_j$ along $\mathbf{R}_{ij}$). As indicated by the maximum FTIR absorption at 1,755 cm^{-1}, the VCD spectra shown in Fig. 4 probe the stretching motions of C=O of carbonyl groups in the PDCG homopolymer, whose transition dipoles are oriented perpendicular to the main-chain backbone (*SI Appendix*, Fig. S7). For PDCG, we observed a so-called split-Cotton effect with a positive VCD band at 1,749 cm^{-1} and a negative one at 1,763 cm^{-1}, indicating the formation of a right-handed helical conformation, with the mirror inverse spectrum for PLCG (20, 21). These same characteristic features appear in VCD spectra of the PCG-based BCPs* (*SI Appendix*, Fig. S8 *A* and *B*), indicating intrachain chirality in the diblock as well. By contrast, VCD measurements of the unpolymerized chiral monomer (HHMA) shows no signal in the C=O stretching region, consistent with the interpretation that signals for Fig. 4*B* and *SI Appendix*, Fig. S4*A* arise from intrachain rotation of the side groups along the chiral PCG backbone. That is, monomeric chirality is transmitted to intrachain conformations, indicating at least some local degree of helical organization of the side groups along the chains in dilute solution.

Hierarchical Organization of Self-Assembled PBnMA-PCG BCPs*. The tendency to form intrachain helical structure is often accompanied by a corresponding tendency for interchain crystallization, an effect that is well documented for chiral PLAs (22, 23). For chiral PLA-based BCP*s, the strong drive for crystallization of the chiral block has been observed to have significant impact on the formation of ordered, microphase separated morphologies. As opposed to well-ordered microdomain morphologies that are typical of equilibrium noncrystalline block–noncrystalline block BCP melts, in solution-cast films of PS-PLLA diblocks, rapid crystallization of the PLLA block (controllable through solvent selectivity and evaporation rate) can lead to crystallization-induced phase separation and the formation of disordered domain structures with little or no detectable trace of chirality at the domain scale (e.g., noncylindrical, semicrystalline morphologies) (14–16). Thus, we first compared the crystallization tendencies of chiral PCG-based polymers to chiral PLA polymers. In *SI Appendix*, Figs. S11 and S12, we compare wide-angle X-ray diffraction (WAXD) and differential scanning calorimetry (DSC) characterization of chiral PLA and chiral PCG homopolymers. Postcasting crystallization of the chiral PLA homopolymers leads to a melting peak at around 168 °C in DSC and a minor exothermic peak during DSC heating (*SI Appendix*, Fig. S12), consistent with observation of sharp diffraction peaks in WAXD (*SI Appendix*, Fig. S11). These Bragg peaks correspond

Table 1. Characterization of chiral PLA homopolymers, chiral PCG homopolymers, PCG-based BCPs*, and PLA-based BCPs*

Code	M_n, achiral block, kg/mol[†]	M_n, chiral block, kg/mol[†]	M_n, total, kg/mol	M_w/M_n[‡]	$f_{PLA}{}^{v}$ or $f_{PCG}{}^{v}$	d,[§] nm	N,[¶] degree of polymerization
PLCG 44	—	44.0	—	1.12	—	—	314
PLCG 16	—	16.0	—	1.12	—	—	114
PLCG 11	—	11.0	—	1.19	—	—	79
PDCG 38	—	38.0	—	1.12	—	—	271
PDCG 17	—	17.0	—	1.14	—	—	121
PDCG 11	—	11.0	—	1.20	—	—	79
PLLA 9.5	—	9.5	—	1.23	—	—	132
PDLA 10	—	10.0	—	1.26	—	—	139
PS-PLLA-1[#]	29.4	18.3	47.7	1.04	0.34	55.7	537
PS-PLLA-2[#]	34.0	27.0	61.0	1.20	0.39	—	702
PBnMA-PDCG	31.0	14.8	45.8	1.08	0.35	43.5	280
PBnMA-PLCG	29.0	15.0	44.0	1.18	0.37	43.2	271

[†]M_n is determined by ^{1}H NMR.
[‡]Molecular-weight polydispersity ($Đ_M$, M_w/M_n) is determined by gel permeation chromatography using standard calibration.
[§]The *d*-spacing is calculated from the first peak of SAXS.
[¶]The degree of polymerization is defined by the total molecular weight of constituent divided by the molecular weight of one chemical repeat.
[#]Data from ref. 9.

Downloaded by guest on January 10, 2020

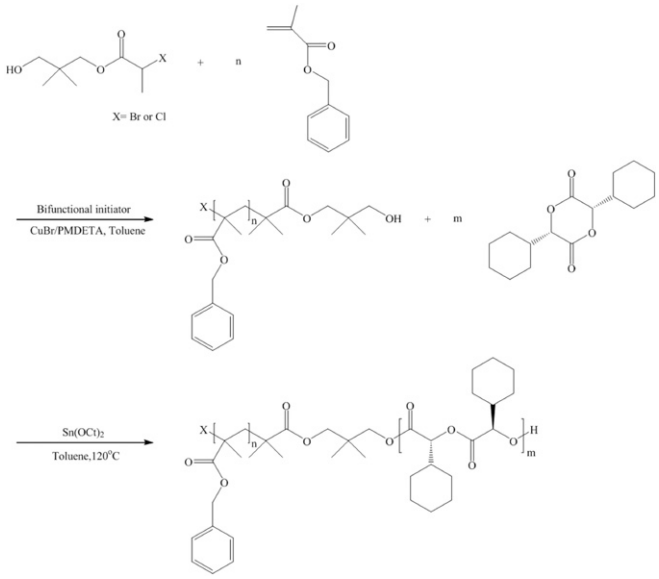

Fig. 2. Synthetic routes of PBnMA-PDCG.

to the (200)/(110) and (203) Bragg peaks of crystalline PLA. By contrast, the WAXD pattern of solution-cast chiral PCG homopolymers (measured at room temperature) shows a scattering pattern typical of an amorphous polymer, while DSC shows no evidence of melting upon heating up to 180 °C. Therefore, although chiral-PCG–based polymers exhibit a measure of intrachain helicity, as probed by VCD, the chiral chain structure does not promote formation of crystalline PCG. It is likely that the intrachain helical structure that is apparently favored by the aromatic side group may not be sufficiently compatible with a low-energy crystal polymorph of PCG due its bulkier size, relative to the methyl side group of PLA polymers, hence promoting intrachain conformational chirality, while largely (if not completely) suppressing crystallization of chiral PCG. As shown in the DSC traces of *SI Appendix*, Fig. S14, the lack of crystallinity of the chiral PCG blocks persists for as-cast films and also for a PBnMA-PCG sample annealed at 180 °C for 5 min.

Given the lack of a competitor semicrystalline state of chiral blocks, the potential for chiral PCG to transfer its chirality to the self-assembled domain morphology of the PBnMA-PCG BCP* can be readily tested by room temperature casting from dichloromethane. Fig. 5 *A* and *B* show the transmission electron microscopy (TEM) bright-field images of PBnMA-PDCG and PBnMA-PLCG, in which discrete PCG microdomains appear bright and the PBnMA matrix appears dark due to the RuO_4 staining. The characteristic "crescent-like" pattern clearly observable in these projections is indicative of the helical the cylinder H* morphology (*SI Appendix*, Fig. S15). The 1D small-angle X-ray scattering (SAXS) patterns PBnMA-PDCG and PBnMA-PLCG in Fig. 5 *B* and *D*, respectively, both show reflections at relative q ratios of $1:\sqrt{3}:\sqrt{4}:\sqrt{7}$, consistent with hexagonally packing of quasitubular domains previously observed for chiral PLA-based BCP*s that have been kinetically trapped in noncrystalline states. The appearance of the H* in the PBnMA-PDCG and a range of previously studied PLA-based diblocks suggests that the formation of the H* phase from BCPs* is generically driven by chirality at the chain scale and is independent of the precise chemical structure of both chiral and achiral components.

While the appearance of helical domain shapes is consistent with a mechanism of chirality transfer from chiral PCG block, 3D tomographic imaging is required to determine the handedness, and test whether the same chirality of the monomeric units is ultimately transferred to the same chirality (in this case, handedness) of the helical domains. We carried out 3D transmission electron microscope tomography (3D TEM) from a tilt-series of TEM images of thin sections of solution cast PBnMA-PCG, with unstained PCG (bright helices) in stained PBnMA (dark matrix). When the long axis of the helical PCG domains are parallel to the tilting axis, the reconstruction is limited by the strong attenuation of contrast of bright PCG domains by the dark PBnMA matrix and the missing wedge of information due to the limitation on the range of available tilt angles. To avoid this problem, we carried out TEM tilt series with the long axis of PCG domains perpendicular to the tilt axis (see *SI Appendix* for further details; *SI Appendix*, Fig. S16). Fig. 6*A* shows the results of the 3D reconstruction of the PBnMA-PLCG and PBnMA-PDCG BCPs* samples. The volume fraction of PCG phase estimated from the 3D reconstruction was ∼0.30, which is only 0.02 different to that calculated result from the block molecular weights and component densities ($f_{PDCG}{}^{v}$ = 0.35 and $f_{PLCG}{}^{v}$ = 0.37). Due to the orthogonal orientation of the helical axis of the domains relative to the microtome section, whose thickness is limited to <200 nm, it was not possible to reconstruct an entire helical repeat of the domain. Instead, we focus only on characterizing the handedness of the H* domains by tracing the helical contour along the pitch axis, along which left- and right-handed helices will experience a counterclockwise rotation and clockwise rotation, respectively (Fig. 6*B*; also see *SI Appendix* for video animation, Movies S1 and S2). As shown in Fig. 6*C*, counterclockwise and clockwise tubular shapes can be identified by the reconstruction images of portions of the helical domains from the PBnMA-PLCG and PBnMA-PDCG samples, respectively. Accordingly, the handedness of the H* in the PBnMA-PDCG is right-handed (H^*_R), whereas the handedness of the H* in the PBnMA-PLCG is left-handed (H^*_L), thus proving the homochiral evolution from intrachain conformational chirality to chirality the of mesodomain shape the PCG-based BCPs*. This relationship we argue must be driven by the presence of chiral intermolecular interactions of some type. Finally, we note that while it is not possible to accurately characterize the helical pitch of the H* domains formed by PBnMA-PCG BCP*s due to limitations of the 3D TEM reconstructions, the pitches are clearly in excess of the ∼200-nm thickness of the microtome section, which is also larger than previously reported values of H* domain pitches formed in kinetically trapped states of PLA-based BCP*s (9). In oSCF results, the final helical pitch of the H* morphology correlates nearly linearly with the preferred pitch of cholesteric segment packing assumed in the model. However, it should be emphasized that the critical value of that inverse pitch for thermodynamic stability of H* is expected to decrease with both segregation strength (χN) and with the twist Frank elastic constant for chiral segments (15).

Thermodynamic Stability of Self-Assembled H* in PBnMA-PDCG. The mean-field model for chiral diblock copolymers put forward by Grason et al. (18, 24) proposes that chirality at the chain scale propagates to the mesodomain assembly through a preference for twist (i.e., cholesteric) packing of chiral block chain segments within the microphase separated state. oSCF studies of the phase diagram are dictated by two parameters: the inverse pitch of preferred cholesteric packing of chiral segments (as in a chiral mesogenic liquid crystal) and degree of segregation strength (24, 25). In particular, for a given chiral- vs. achiral-block composition, when the inverse pitch, the twist Frank elastic constant, and degree of segregation strength exceed critical values, H* becomes thermodynamically stable relative to other domain patterns (e.g., achiral DG and L). A predictive physical model for the nature and magnitude of chiral intersegment forces in a melt-state packing of chiral-PLA remains unclear, the equilibrium stability of H* in a model that assumes preferred cholesteric twisting of chiral block

Downloaded by guest on January 10, 2020

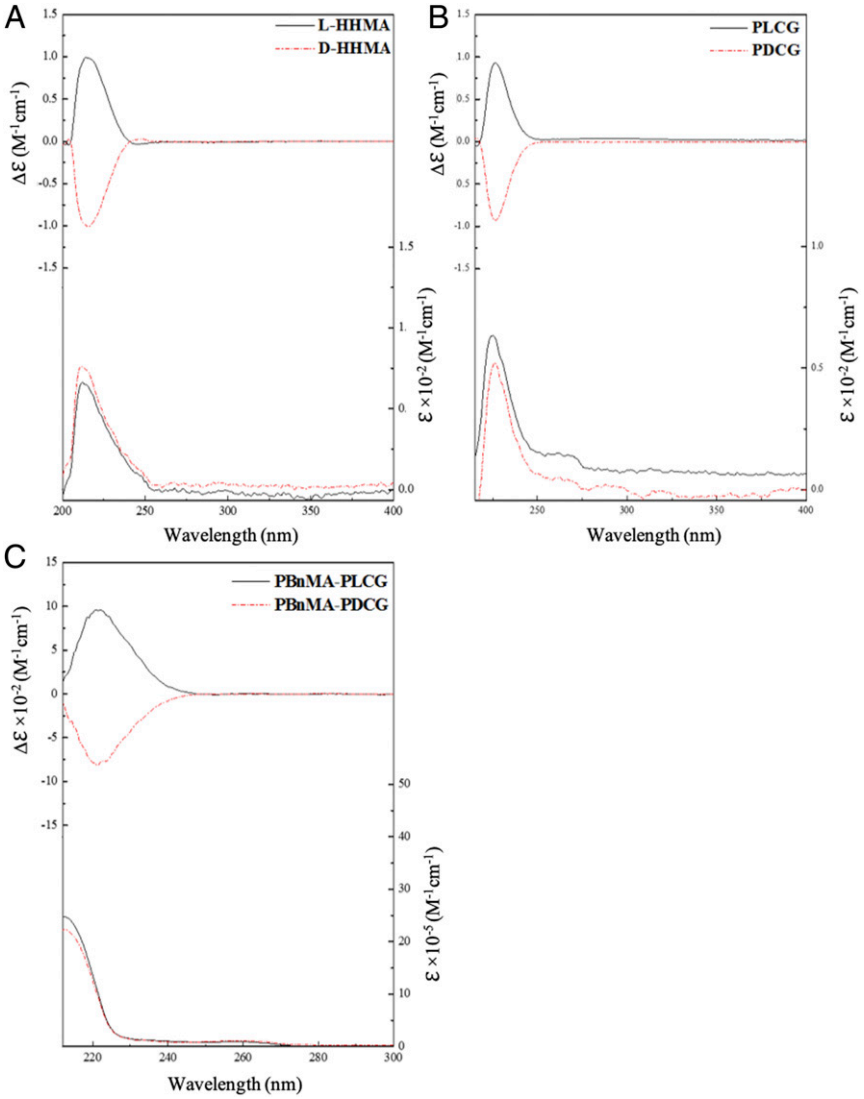

Fig. 3. ECD and corresponding UV-Vis absorption spectra of (*A*) hexahydromandelic acids in dilute THF solution, (*B*) PCG homopolymers in dilute dichloromethane solution, and (*C*) PCG-based BCPs* in dilute *p*-dioxane solution. Concentration of the solution is 0.1 wt%.

segments in refs. 24 and 25, in combination with observations of H* in chiral-PLA based diblocks, is suggestive that chain chirality in these experimental systems propagates to effective segment interactions that favor a pattern of cholesteric twist in the PLA domains. For example, the existence of at least transient and handed helical conformations along the chain backbone leads to a natural hypothesis that effective Kuhn segments of chiral flexible chains (18), like chiral PLA, give rise to at least a modest thermodynamic bias for skew packing of adjacent segments in a microdomain with a handedness that reflects helicity of the backbone within segments, not unlike the generic preference of chiral rod-like liquid crystals for cholesteric order (26, 27).

As noted above, previous experiments on PLA-based BCPs* have shown H* in these systems to be a long-lived metastable phase exhibiting a transformation from H* to DG or to an achiral hexagonal cylinder (HC) phase (9), after long-time annealing at high temperature (above the melting point of PLA). For comparison, we carried out long-time annealing (1 month at 160 °C) of PBnMA-PDCG films. No transition to the DG phase was observed by SAXS (*SI Appendix*, Fig. S17*B*). The 1D SAXS profile shows that the reflections, while sharper due to the annealing treatment, remain at the relative q values of $1:\sqrt{3}:\sqrt{4}:\sqrt{7}$, indicating the enhancement on the long-range order of the hexagonally packed helices; relative first q values are same, suggesting that the domain sizes are same before and after long-time thermal annealing. As shown in *SI Appendix*, Fig. S17*A*, the bright-field TEM image is similar to Fig. 5*A*, and there are no other recognizable projections apparent that would suggest DG, HC, or L phases.

Notably, from the calculated results of chemical group (CG) contributions (see *SI Appendix* for details; *SI Appendix*, Table S2), the difference of solubility parameters (at 25 °C) between two constituted blocks of PBnMA-PDCG is nearly equivalent to PS-PDLA, suggesting that perhaps the two effective χ values during the solvent casting process are also similar. Because segregation strength in BCP derives from the product of χ and degree of polymerization and PCG diblocks possess relatively fewer repeats than previously studied PLA diblocks (*SI Appendix*, Table S2), comparison with the oSCF phases diagram for chiral diblocks would then suggest that the increased stability of H* in PCG-based BCP*s (i.e., its manifestation as a truly equilibrium phase) must derive from the enhancement of chiral intermolecular forces in this chiral polymer, relative to PLA-based BCP*s, which exhibits only a metastable H*. Motivated by this hypothesis, we next consider how different spectroscopic measures of chirality

Downloaded by guest on January 10, 2020

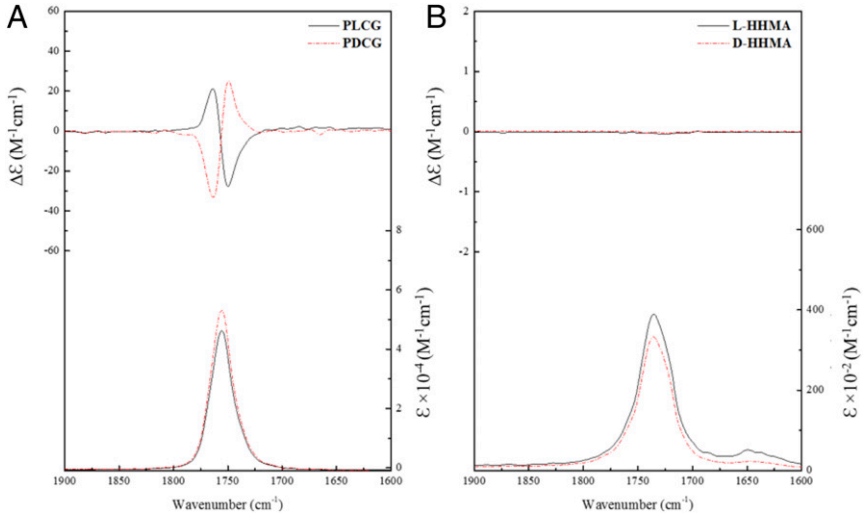

Fig. 4. VCD and corresponding FTIR absorption spectra of (*A*) PCG homopolymers in dilute dichloromethane solution and (*B*) HHMAs in dilute THF solution.

in PCG- and PLA-based BCP*s can be compared to assess possible differences in the strengths of putative chiral interactions that underlie the formation of mesochiral domain patterns.

Comparing Chirality at the Monomeric Level. As described above, in both PLA- and PCG-based BCP*s, chirality at the monomeric level is shown to transfer up to helicity of the intrachain conformation and, ultimately, propagates to the formation and handedness selection of H* domains at the multichain scale. Here, we quantify the "degree of chirality" in both chiral homopolymers via the examined ECD spectra, which quantifies chiral structure and response on the scale of monomeric units. The rotational strength, R, resulting from an excitation of a single chiral chromophore can be predicted based on the electric ($\boldsymbol{\mu}$) and the magnetic ($\mathbf{m}$) moments associated with electronic excitations (between ground and excited states) as the imaginary part of $\boldsymbol{\mu} \cdot \mathbf{m}$ (20). For comparison, the rotational strength can be extracted from ECD measurements from the dissymmetry factor (g factor) (Eq. **1**):

$$g = \Delta\varepsilon/\varepsilon \ldots, \qquad [1]$$

$$g = 4R/D \ldots, \qquad [2]$$

where $\Delta\varepsilon$ is the measured circular dichroism (ε_L-ε_R), ε is the absorptivity of compound, R is the rotational strength, and D is the dipole strength: $D = 9.18 \times 10^{-39} \int(\varepsilon/\lambda)\mathrm{d}\,\lambda$.

From the point of view of chemical structure, the chiral PCG with a larger substituent group (i.e., cyclohexane group) might reasonably be expected to give a larger rotational strength measure of chirality than chiral PLA with a relative compact methyl side group. To test this, we first note that the effect of molecular weight is a critical factor that might influence the intensity of the ECD signal, and confirm that circular dichroism saturates for PCG and PLA homopolymers for molecular weights in excess of 16,000 g/mol and 9,000 g/mol, respectively (*SI Appendix*, Figs. S18 and S19). As a result, the molecular weight of the chiral PCG and PLA homopolymers used for the calculation of the rotational strength was over 16,000 g/mol and 9,000 g/mol.

As shown in Fig. 7, the g factor [which is calculated from the intensities of the ECD signals ($\Delta\varepsilon_{max}$)] from the PLCG per chiral entity is larger than the absorption intensities of the PLLA per molecule. Similar results can also be found for the PDLA and PDCG. The dipole strengths are 10.1×10^{-40} esu^2·cm^2, 9.3×10^{-40} esu^2·cm^2, 5.9×10^{-40} esu^2·cm^2, and 6.2×10^{-40} esu^2·cm^2 for PLCG, PDCG, PLLA, and PDLA, respectively. Accordingly, the rotational strength of PLCG per repeating unit calculated from g factor is 15.2×10^{-40} esu^{2}cm^2, whereas that of PLLA is 7.5×10^{-40} esu^2·cm^2. Also, the rotational strength of PDCG per unit is -14.1×10^{-40} esu^2·cm^2, while that of PDLA is -7.3×10^{-40} esu^2·cm^2. These results show the rotational strength of chiral PCGs is approximately two times larger than that of chiral PLA, confirming that, at the monomeric level, the bulkier side group of the former polymer leads to a significant enhancement of measured chirality. We postulate that this stronger measure of monomer-scale

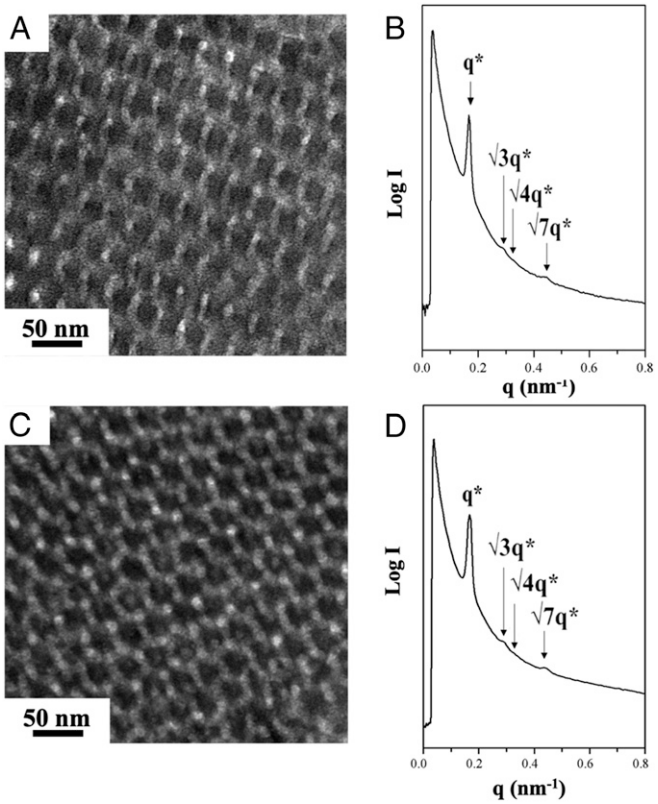

Fig. 5. (*A* and *C*) TEM micrographs and (*B* and *D*) corresponding 1D SAXS profiles of PBnMA-PDCG and PBnMA-PLCG, respectively.

Downloaded by guest on January 10, 2020

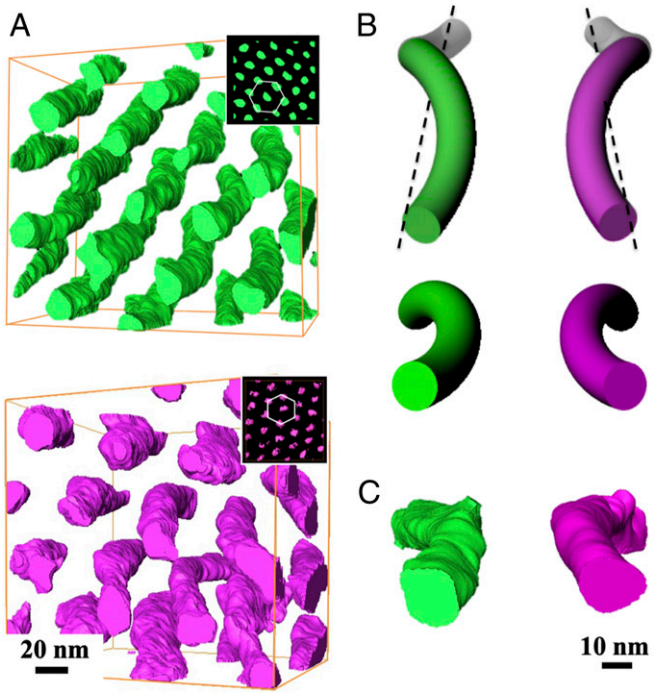

Fig. 6. (*A*) Three-dimensional TEM reconstruction of helical domains from PBnMA-PLCG (*Top*) and PBnMA-PDCG (*Bottom*) BCPs*. *Inset* images show the hexagonal packing of helical nanoarrays viewed along the helical axis. (*B*) Schematic models of counterclockwise (*Left* side) and clockwise (*Right* side) left- and right-handed helical domains. (*C*) Left-handed (*Left* side) and right-handed (*Right* side) helical nanostructure (i.e., H^*_L and H^*_R) reconstructed from PBnMA-PLCG and PBnMA-PDCG BCPs*.

chirality in combination with presumably stronger intrachain interactions between bulky side groups of PCG leads to a more persistent helical bias in the intrachain chiral conformations of chiral PCG over that of chiral PLA, an effect that, in turn, may enhance the chiral anisotropy of intersegment forces in the melt, as we discuss further below.

Intermolecular Chiral Interactions. According to the mean-field model of BCP* melts put forward by Grason and coworkers (24), the coupling between chirality and mesodomain formation, which ultimately stabilizes an equilibrium H* phase, derives from a thermodynamic preference for handed cholesteric twist of the chiral block segments. If, and how precisely, the chirality at the scale of backbones gives rise to such "chiral mesogenic" intersegment forces, remains an important and unanswered question (18). One plausible mechanism is the promotion of at least transient (chiral) helical conformations along distinct chains (and corresponding helical arrangements of interacting groups) that gives rise to steric and/or enthalpic interactions between segments that favors handed skew (much like coiled coils of polypeptide helices) (28). In the absence of a direct experimental measure of intersegment chiral skew, we propose that increases in chirality measured at the intrachain scale that reflect tighter or more persistent helical structure along the chain might naturally be expected to correlate with stronger preference for chiral intersegment skew, specifically a shorter preferred intersegment pitch (measured relative to the size of an equivalent ideal polymer coil). This scenario is consistent with the observation of higher rotational strength of chiral PCGs than chiral PLAs, as well as the apparently enhanced thermodynamic stability of the mesochiral H* phase in PCG-based BCP*s in contrast to the metastable H* phase observed PLA-based BCP*s. That is, on the basis of the comparison mean-field theory of chiral diblocks and these experimental results, it is reasonable to speculate that the intermolecular chiral interactions between chiral PCGs should be larger than the one from chiral PLAs. This scenario implies the existence of at least some weak measure of liquid-crystalline (LC) segmental order within the chiral domains of BCP* morphologies exists, with perhaps, an enhanced degree of LC order in PCG-based systems.

We therefore probe the possibility of LC segmental order of PCG materials using DSC and polarized light microscopy, techniques that do not, at present, give evidence of any explicit (e.g., thermotropic or lyotropic) LC transition in PCG. There is no obvious enthalpic peak from the DSC measurements of chiral PCG homopolymer and PCG-based BCPs*, perhaps an indication implying that a thermotropic LC transition is not apparent due to a relatively short persistence length of PCG, or instead that the clearing point exceeds 200 °C and PCG retains a relatively weak LC over this range (notably, the 5% degradation temperature is ~253 °C, as shown in *SI Appendix*, Fig. S13). Moreover, scattering experiments [i.e., wide-angle X-ray scattering (WAXS)] were conducted but no mesophase characteristic signature can be identified in the patterns. While melt BCPs are typically described as "amorphous," microphase separation necessarily introduces anisotropy in the packing of segments as measured by nonvanishing orientational order parameters (29), even in the absence of strong orientational interactions between segments (i.e., interactions which would give rise to thermotropic isotropic/nematic transitions). Therefore, microphase separation, which induces at least some measure of orientational order of segments within the domain, has the effect of enhancing or amplifying otherwise weakly anisotropic tendencies of intersegment forces between segments (30), such as intersegment forces that favor twisted (cholesteric) packing. The intrinsic

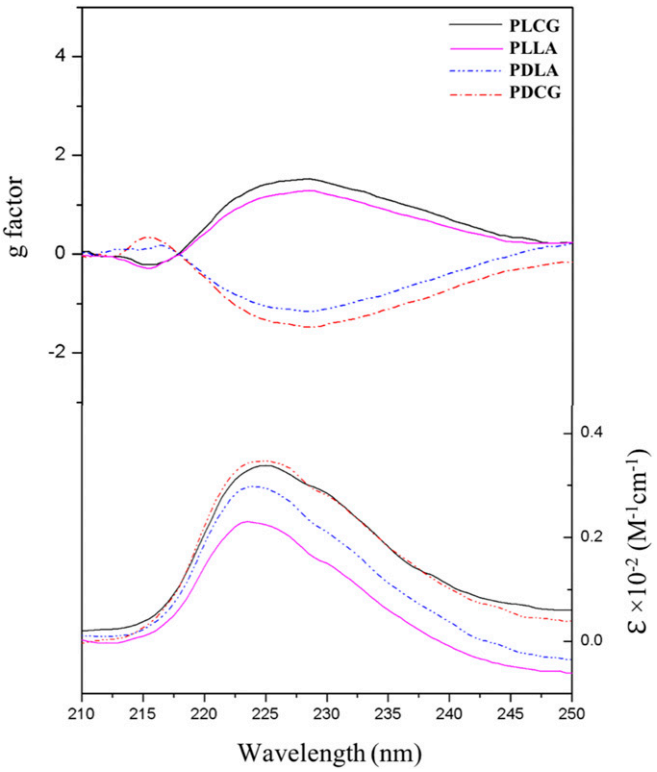

Fig. 7. ECD and corresponding UV-Vis absorption spectra of various molecular weight of chiral PLAs and chiral PCGs in dichloromethane dilute solution. The concentration of solution is 0.1 wt% (M_n = 9,500 g/mol for PLLA, 10,000 g/mol for PDLA, 16,000 g/mol for PLCG, and 17,000 g/mol for PDCG).

Downloaded by guest on January 10, 2020

coupling between microphase separation and segmental anisotropy may thus account for how intersegment chiral forces may be sufficiently strong to promote mesodomain chirality, notwithstanding a clear signature of any thermotropic (lyotropic) LC ordering in PCG- or PLA-based BCPs*.

In the absence of direct evidence of intersegment twisting, we search for evidence of intermolecular chiral interactions of the PCG polymer chains using VCD. VCD spectra in the range of 1,700 cm^{-1} indicate the intrachain helicity observed in solution (Fig. 8*A*) persists in cast films of chiral PGC homopolymers (Fig. 8*C*). As above, the split-type Cotton effect correlates with handed helical (intrachain) conformation of ester groups (C=O stretching within chiral PCG). Again, this is because VCD signal arises from interchromophore conformations in proportion to $\Delta_{ij} = (\boldsymbol{\mu}_i \times \boldsymbol{\mu}_j) \cdot \mathbf{R}_{ij}$ (20), and the fact that $\boldsymbol{\mu}_i$ and $\boldsymbol{\mu}_j$ are perpendicular to the chain backbone (*SI Appendix*, Fig. S7). To probe the possible existence of chiral anisotropic forces between segments on different chains, it is therefore necessary to probe excitations whose dipoles are predominantly parallel to the main chain, so that nonvanishing averages of Δ_{ij} imply chiral skew between adjacent backbones. Thus, we examined the optical activities of C–O–C vibration by VCD to assess the intermolecular chiral interactions because the transition dipole moment of this group in nearly parallel to the backbone of chiral PCG (*SI Appendix*, Fig. S7) (31, 32). The VCD signals that probe C–O–C vibration, in the wavelength range of 1,100–1,300 cm^{-3}, are shown from chiral PCG homopolymers in Fig. 8 *B* and *D*, at 2 wt% in THF and cast films, respectively. Due to the orientation of the C–O–C dipole, the VCD signals are taken as an indication of bias in the skew orientation of segments on different PCG chains, presumably driven by intermolecular forces that reflect the chiral structure of the PCG chains. Note that a simple estimate for the PCG solution suggest it to be 1/7 of the overlap concentration, and hence, we cannot separate the contributions to the VCD signal coming from contacts between segments on unlike chains (infrequent) from the contributions that arise from segment–segment contact of distant chain portions with a given coil (relatively more frequent). By contrast, no such VCD signal can be observed for the chiral PLAs, suggesting any such chiral interchain may be much weaker in PLA than in PCG (*SI Appendix*, Fig. S20).

Note that, for the identification of absorption peaks in C–O–C regions, the IR absorption peaks of the chiral PCGs were assigned in comparison with the chiral PLAs since there are fewer detailed studies of IR absorption of the chiral PCGs (33). *SI Appendix*, Fig. S21 shows the FTIR absorption spectra of

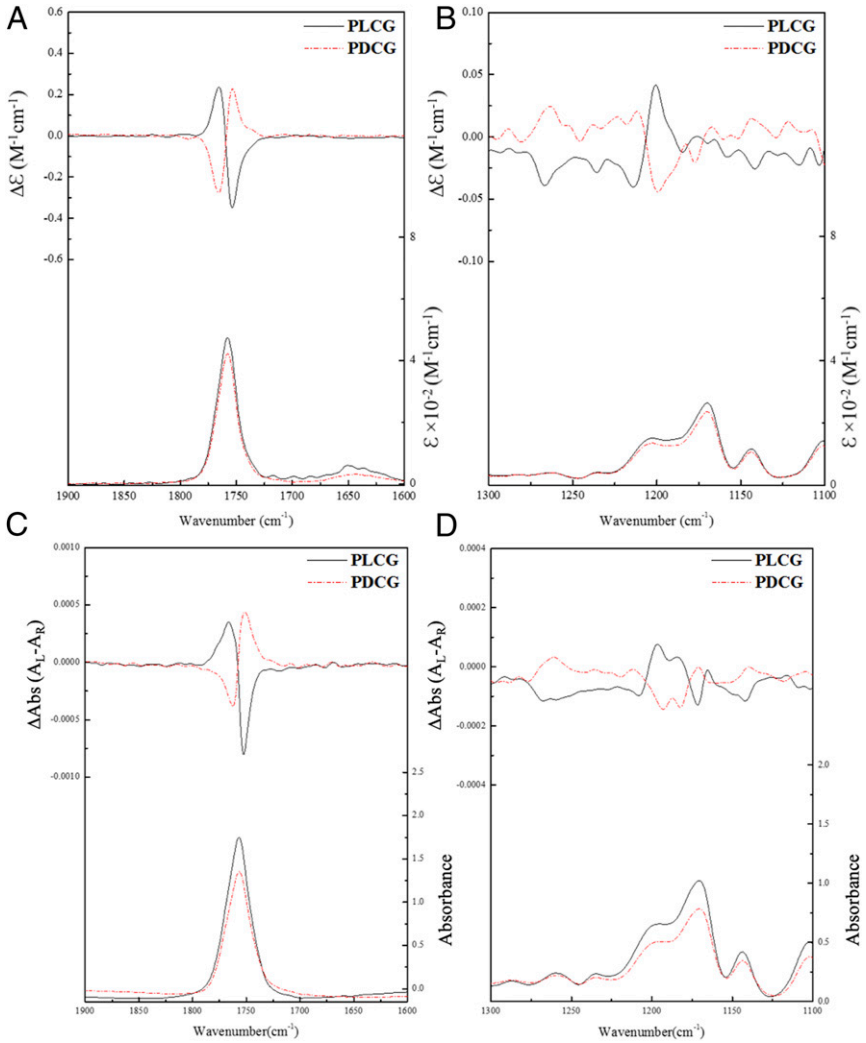

Fig. 8. VCD and corresponding FTIR absorption of (*A*) C=O and (*B*) C–O–C vibration in chiral PCGs in THF solution. The concentration of the solution is 2 wt%. VCD and corresponding FTIR absorption of (*C*) C=O and (*D*) C–O–C vibration in the chiral PCGs in the solid state after solution casting.

Downloaded by guest on January 10, 2020

PLCG and PLLA, and the appearances of absorption spectra in PLCG and PLLA are quite similar to each other (see *SI Appendix* for details; *SI Appendix*, Fig. S21). According to a previous study of crystallized chiral PLAs, the VCD signals in the absorption bands of the C–O–C vibration are silent in the amorphous state, with strong VCD signals appearing only upon crystallization (31). In the case of crystalline PLLA, this signal was interpreted as evidence of strong interactions between groups on distinct chains whose geometry reflects a chiral symmetry, for example, interactions between helically distributed side groups on parallel stems. Note that the intermolecular interactions will not be induced by the crystallization in chiral PCGs system since the crystallization in chiral PCGs is essentially eliminated by its bulky side group, and WAXD and DSC suggest that PCGs remain in an amorphous, or at most, a weakly LC state. Moreover, it is noted that the VCD signals might result from anisotropic orientation of polymeric chains, giving artificial VCD signals, particularly in the bulk state and thin-film state. To clarify the origins of the VCD signals, following Kuroda et al. (34) and Buffeteau et al. (35), we carried out VCD on bulk solution cast (with 180 °C for 3 min) samples at sample orientations of 0° and 90°. As shown in *SI Appendix*, Fig. S22, the VCD signals of chiral PCGs at 0° and 90° appear similar, indicating that any anisotropic effects on VCD measurement are insignificant. As a result, there is no significant effect of linear dichroism (LD) and linear birefringence (LB) on the VCD results. Namely, the induced VCD signals are intrinsic VCD signals that are attributed to asymmetric packing of the chiral PCGs. In contrast to the chiral PLAs in the amorphous state (31), the VCD signals in the absorption band of C–O–C region become significant, reflecting that the chiral PCGs indeed have stronger intermolecular chiral interactions than chiral PLAs. While this VCD signal is not a result of strong interactions induced by crystallinity, its appearance is suggestive of strong chain–chain interactions that reflect a chiral symmetry, such as would be the case of interactions between helically distributed side groups that drive cholesteric order chiral polymers (28). Accordingly, we speculate that such chiral interchain forces observed in PCG homopolymers all favor some measure of twisted (cholesteric) segment packing in microphase separated BCP*, consistent with the mechanism that drives equilibrium H* phases in the mean-field model of chiral diblocks. Detailed intrinsic quantitative measurements with bond angles, twisting angles of the chemical structures, and interchain and intramolecular chiral geometry are still under investigation and will be discussed in a future report.

Conclusions

The possibility of universal behaviors for self-assembly of BCPs* that traces from monomeric chirality was explored through the synthesis and characterization of a chiral block copolymer system, PBnMA-PCG BCP*. The bulky cyclohexyl group of the PCG essentially eliminates the crystallization of the chiral block, enabling the formation of an equilibrium H* phase from self-assembled PBnMA-PCG BCPs*. The homochiral evolution from monomeric, to conformational, and to mesodomain chirality is evidenced by probes of chiral structure in self-assembled PBnMA-PCG BCPs* across multiple size scales. Moreover, we observe a higher rotational strength of chiral PCG chain than that of chiral PLA chain as evidenced by the ECD g-factor results at C=O absorption region, which is consistent with the observation of a thermodynamically stable H* phase. Indeed, oSCF studies of chiral diblock melts suggest that stronger intersegment chirality enhances the stability of mesochiral H*. Also, VCD spectra of chiral PCG in C–O–C absorption region point to the existence of intersegment skew in the BCP* morphology. Taken together, we postulate that the bulkier chiral side group of PCG may give rise to a more persistent helical bias, which in turn enhances the chiral anisotropy of intersegment forces that favor the formation of chiral mesodomain morphologies.

Materials and Methods

Polymer Syntheses. The detailed procedures for syntheses of PCG-based polymers and BCPs can be found in *SI Appendix*.

Sample Preparation. Bulk samples were prepared by solution casting from dichloromethane (CH_2Cl_2) at room temperature. The solubility parameters (δ) of each component at 25 °C are as follows: $\delta_{CH2Cl2} = 9.93$ $(cal{\cdot}cm^{-3})^{1/2}$, $\delta_{PS} = 9.0$ $(cal{\cdot}cm^{-3})^{1/2}$, $\delta_{PDLA} = 10.25$ $(cal{\cdot}cm^{-3})^{1/2}$, $\delta_{PBnMA} = 10.04$ $(cal{\cdot}cm^{-3})^{1/2}$, and $\delta_{PDCG} = 8.71$ $(cal{\cdot}cm^{-3})^{1/2}$; as a result, dichloromethane is a slightly selective solvent for PDLA and PBnMA. Samples were first dissolved in CH_2Cl_2 at a concentration of 10 wt%. After the sample was completely dissolved in dichloromethane, the solution was filtrated through a filter with 0.45-μm pores to remove the impurities. The solution was then transferred in a vial and sealed well by aluminum foil. Small punch holes in the foil allowed for the evaporation of the solvent over 1 wk. Subsequently, the bulk samples were heated to 180 °C for 3 min to eliminate the thermal history from solution casting, and then rapidly cooled at a rate of 150 °C/min to room temperature, giving the self-assembled phase without the effect of crystallization.

Characterization. DSC experiments were carried out in a Perkin-Elmer DSC 7 with temperature and heat flow scales at constant heating rates (10 °C/min) carefully calibrated with standards. The DSC samples were first annealed for 3 min at $T_{max} = 180$ °C. They were then rapidly cooled at 150 °C/min to room temperature and heated again to T_{max} to determine T_g and explore for a possible T_m; note that the PLLA and PDLA will experience cold crystallization during heating, whereas no crystallization event can be found in the PLCG and PDCG during heating.

UV-Vis and ECD spectra were performed using a JASCO J-815 spectrometer. Solution samples for ECD measurement were placed in a cylindrical quartz cell with a light path of 1.0 mm. FTIR absorption and corresponding VCD spectra were acquired using a JASCO FVS-6000 spectrometer. Solution samples for VCD measurement were placed in a cylindrical CaF_2 cell with a light path of 50 μm. Solutions for chiroptical measurements were 0.1 wt% in dichloromethane for ECD and 1 wt% in dichloromethane for VCD measurements. Solid film samples were obtained from dichloromethane drop casting with thermal treatment (180 °C, 5 min) to remove the thermal history with the cooling rate 150 °C/min.

Bright-field TEM images were obtained using a JEOL JEM-2100 LaB_6 transmission electron microscope (at an accelerating voltage of 200 kV). Bulk samples could be sectioned at room temperature using a Leica Ultramicrotome because the T_g of PBnMA and PCG are 70 °C and 100 °C, respectively. Then the microsections were collected on copper grids. Staining was accomplished by exposing the samples to the vapor of a 4% aqueous RuO_4 solution for 1 h to enhance the mass-thickness contrast for TEM observation. For electron tomography (3D TEM) experiments, the microsections were collected on copper grids (100 mesh) covered with a polyvinyl formal film (thickness, ~40 nm). To achieve the image alignment for electron tomography, fiducial gold markers (diameter, 10 nm; purchased from Polysciences) were homogeneously distributed over the microsections. Subsequently, the sample was covered by a thin layer of carbon (thickness, ~2 nm) via vacuum sputtering to enhance the electron conductivity and to minimize the radiation damage during the collection of projections at different tilting angles. A series of 121 TEM images were collected from –60 to +60° tilt angles at an angular interval of 1°. Images were recorded on a Gatan CCD camera. Alignment of the tilt series and 3D reconstruction were performed by using IMOD software. The reconstructed volume was then filtered by using a $5 \times 5 \times 5$ median filter for noise reduction. Avizo 7.1.1 (Visualization Sciences Group) was then used to trim the filtered volume keeping only the volume of interest for further analyses. Consequently, 3D analyses, such as binarization, segmentation, rotation, and visualization, of the volume of interest were achieved by using Avizo 7.1.1.

SAXS experiments were conducted at the synchrotron X-ray beamline 23A1 at the National Synchrotron Radiation Research Center in Hsinchu, Taiwan. Data were collected with a Dectris Pilatus 1M-F area detector to cover the q ranges from 0.003 to 0.2 $Å^{-1}$ with a 0.5-mm diameter X-ray beam of 10 keV (wavelength $\lambda = 1.24$ Å). For SAXS measurement, bulk samples of the BCPs were first heated to 180 °C for 3 min to eliminate the thermal history resulting from sample preparation, and then rapidly cooled at a rate of 150 °C/min to room temperature. All of the SAXS experiments were carried out at room temperature. Wide angle X-ray diffraction (WAXD) results were obtained by a Rigaku Multiflex 2-kW automated diffractometer using CuKα radiation (0.1542 nm). The samples were scanned across a 2θ range of 5–30° at a 1°/min scanning rate. The peak positions were calibrated using silicon powder in the high-angle region (>15°) and

Downloaded by guest on January 10, 2020

silver behenate in the low-angle region (<15°). For WAXD measurements, the as-casting samples were prepared with the same procedure as mentioned in sample preparation section to investigate the crystallization behavior after solution casting. All of the WAXD experiments were carried out at room temperature.

ACKNOWLEDGMENTS. We thank the Ministry of Science and Technology (MOST), Taiwan, for financially supporting this research under Contracts MOST 103-2221-E-007-132 -MY3 and MOST 106-2119-M-007-010, and the Air Force Office of Scientific Research (United States) under Asian Office of Aerospace Research and Development Award 15IOA107.

1. Lehn JM (1985) Supramolecular chemistry: Receptors, catalysts, and carriers. *Science* 227:849–856.
2. Whitesides GM, Grzybowski B (2002) Self-assembly at all scales. *Science* 295: 2418–2421.
3. Neville AC (1993) *Biology of Fibrous Composites. Development Beyond the Cell Membrane* (Cambridge Univ Press, Cambridge, UK).
4. Sharma V, Crne M, Park JO, Srinivasarao M (2009) Structural origin of circularly polarized iridescence in jeweled beetles. *Science* 325:449–451.
5. Li L, Weaver JC, Ortiz C (2015) Hierarchical structural design for fracture resistance in the shell of the pteropod *Clio pyramidata*. *Nat Commun* 6:6216.
6. Fratzl P (2007) Biomimetic materials research: What can we really learn from nature's structural materials? *J R Soc Interface* 4:637–642.
7. McPhedran R, Park A (2015) Biomimetics: Lessons on optics from nature's school. *Phys Today* 68:32–37.
8. Matsen MW (2002) The standard Gaussian model for block copolymer melts. *J Phys* 14: R21–R47.
9. Ho RM, et al. (2009) Block copolymers with a twist. *J Am Chem Soc* 131:18533–18542.
10. Ho RM, Chiang YW, Lin SC, Chen CK (2011) Helical architectures from self-assembly of chiral polymers and block copolymers. *Prog Polym Sci* 36:376–453.
11. Ho RM, et al. (2012) Transfer of chirality from molecule to phase in self-assembled chiral block copolymers. *J Am Chem Soc* 134:10974–10986.
12. Wen T, Wang HF, Li MC, Ho RM (2017) Homochiral evolution in self-assembled chiral polymers and block copolymers. *Acc Chem Res* 50:1011–1021.
13. de Gennes PG, Prost J (1995) *The Physics of Liquid Crystals* (Clarendon Press, Oxford).
14. Chiang YW, Ho RM, Thomas EL, Burger C, Hsiao BS (2009) A spring-like behavior of chiral block copolymer with helical nanostructure driven by crystallization. *Adv Funct Mater* 19:448–459.
15. Zhao W, Chen D, Grason GM, Russell TP (2013) Formation of H* phase in chiral block copolymers: Effects of solvents and solution-cast conditions. *Macromolecules* 46: 455–462.
16. Zhao W, et al. (2013) Formation of H* phase in chiral block copolymers: Morphology evolution as revealed by time-resolved X-ray scattering. *Macromolecules* 46:474–483.
17. Chen CC, et al. (2010) Single helix to double gyroid in chiral block copolymers. *Macromolecules* 43:8637–8644.
18. Grason GM (2015) Chirality transfer in block copolymer melts: Emerging concepts. *ACS Macro Lett* 4:526–532.
19. Jing F, Smith MR, III, Baker GL (2007) Cyclohexyl-substituted polyglycolides with high glass transition temperatures. *Macromolecules* 40:9304–9312.
20. Nakanishi K, Berova N, Woody RW (1994) *Circular Dichroism: Principles and Applications* (VCH Press, New York).
21. Holzwarth G, Chabay IJ (1972) Optical activity of vibrational transitions: A coupled oscillator model. *J Chem Phys* 57:1632–1635.
22. Cartier L, Okihara T, Lotz B (1997) Triangular polymer single crystals: Stereocomplexes, twins, and frustrated structures. *Macromolecules* 30:6313–6322.
23. Lotz B (2012) Frustration and frustrated crystal structures of polymers and biopolymers. *Macromolecules* 45:2175–2189.
24. Zhao W, Russell TP, Grason GM (2013) Chirality in block copolymer melts: Mesoscopic helicity from intersegment twist. *Phys Rev Lett* 110:058301.
25. Goodby JW (1991) Chirality in liquid crystals. *J Mater Chem* 1:307–318.
26. Straley JP (1976) Theory of piezoelectricity in nematic liquid crystals, and of the cholesteric ordering. *Phys Rev A* 14:1835–1841.
27. Harris AG, Kamien RD, Lubensky TC (1999) Molecular chirality and chiral parameters. *Rev Mod Phys* 71:1745–1757.
28. Samulski TV, Samulski ET (1977) van der Waals-Lifshitz forces in lyotropic polypeptide liquid crystals. *J Chem Phys* 67:824–830.
29. Prasad I, Seo Y, Hall LM, Grason GM (2017) Intradomain textures in block copolymers: Multizone alignment and biaxiality. *Phys Rev Lett* 118:247801–247806.
30. Burke CJ, Grason GM (2018) Intradomain phase transitions in flexible block copolymers with self-aligning segments. *J Chem Phys* 148:174905.
31. Wang HF, et al. (2017) Handedness of twisted lamella in banded spherulite of chiral polylactides and their blends. *Macromolecules* 50:5466–5475.
32. Li MC, Wang HF, Chiang CH, Lee YD, Ho RM (2014) Lamellar-twisting-induced circular dichroism of chromophore moieties in banded spherulites with evolution of homochirality. *Angew Chem Int Ed Engl* 53:4450–4455.
33. Kister G, Cassanas G, Vert M (1998) Effects of morphology, conformation and configuration on the IR and Raman spectra of various poly(lactic acid)s. *Polymer* 39: 267–273.
34. Kuroda R, Harada T, Shindo Y (2001) A solid-state dedicated circular dichroism spectrophotometer: Development and application. *Rev Sci Instrum* 72:3802–3810.
35. Buffeteau T, Lagugné-Labarthet F, Sourisseau C (2005) Vibrational circular dichroism in general anisotropic thin solid films: Measurement and theoretical approach. *Appl Spectrosc* 59:732–745.

Downloaded by guest on January 10, 2020